CHIN. PHYS. LETT. Vol. 38, No. 5 (2021) 057302

Nonlinear Hall Effect in Antiferromagnetic Half-Heusler Materials

Cheng Chen(陈诚)[1†], Huaiqiang Wang(王怀强)[1†], Zhilong Yang(杨志龙)[1], and Haijun Zhang(张海军)[1,2*]

[1]*National Laboratory of Solid State Microstructures, School of Physics, Nanjing University, Nanjing 210093, China*
[2]*Collaborative Innovation Center of Advanced Microstructures, Nanjing University, Nanjing 210093, China*

(Received 7 January 2021; accepted 5 March 2021; published online 2 May 2021)

It has recently been demonstrated that various topological states, including Dirac, Weyl, nodal-line, and triple-point semimetal phases, can emerge in antiferromagnetic (AFM) half-Heusler compounds. However, how to determine the AFM structure and to distinguish different topological phases from transport behaviors remains unknown. We show that, due to the presence of combined time-reversal and fractional translation symmetry, the recently proposed second-order nonlinear Hall effect can be used to characterize different topological phases with various AFM configurations. Guided by the symmetry analysis, we obtain expressions of the Berry curvature dipole for different AFM configurations. Based on the effective model, we explicitly calculate the Berry curvature dipole, which is found to be vanishingly small for the triple-point semimetal phase, and large in the Weyl semimetal phase. Our results not only put forward an effective method for the identification of magnetic orders and topological phases in AFM half-Heusler materials, but also suggest these materials as a versatile platform for engineering the nonlinear Hall effect.

DOI: 10.1088/0256-307X/38/5/057302

Since the discovery of the topological nature of the quantum Hall effect,[1] many topological states and topological materials, including topological insulators,[2−7] topological semimetals,[8−15] topological superconductors,[16−21] topological magnetic axion insulators,[22−28] and so on, have been found, which has significantly improved our understanding of symmetry and topology in condensed matter physics. Quasiparticle excitations near certain band crossing points, protected by specific space-group symmetries,[29,14] can be considered as analogs of elementary particles, such as Dirac and Weyl quasiparticles; these materials are known as Dirac and Weyl semimetals.[8,10] As typical topological materials, half-Heusler compounds have attracted widespread attention. Both topological insulators and topological semimetals have been discovered in half-Heusler compounds, both with and without external perturbations such as strains and magnetic fields.[13,30−38] Intriguingly, it has recently been shown that in the presence of the antiferromagnetic (AFM) order, rich magnetic topological phases can emerge in AFM half-Heusler materials, including AFM topological insulators, Dirac/Weyl semimetals, nodal-line semimetals, and triple-point (TP) semimetal phases.[22,38−40] This indicates that AFM half-Heusler materials could be a versatile platform from which researchers can study magnetic topological states. Since magnetic topological states depend on a detailed AFM configuration, the problem of how to distinguish magnetic topological states in AFM half-Heusler materials turns out to be a significant issue.

Topologically nontrivial states usually manifest via unique transport behaviors, such as quantized Hall conductivity for the quantum Hall effect with broken time-reversal symmetry.[41,7] Recently, a second-order nonlinear Hall effect (NLHE) was proposed in relation to noncentrosymmetric materials in the presence of the time-reversal symmetry,[42] which essentially originates from the Berry curvature dipole (BCD) of electronic structures. Moreover, the NLHE has also been predicted in transition metal dichalcogenides[43−45] and Weyl semimetals.[42,46−48] Shortly after this, the NLHE was experimentally observed.[49−52] As such, the NLHE offers an effective approach to the characterization of topological states. It is worth mentioning that the NLHE has been extended to include AFM materials[53] with $\mathcal{S} = \mathcal{T}\tau_{1/2}$ symmetry, i.e., a combination of time-reversal symmetry $\mathcal{T}$ and a fractional translation $\tau_{1/2}$. Since the BCD is present even under $\mathcal{S}$ symmetry, it plays a similar role to time-reversal symmetry $\mathcal{T}$. This therefore allows us to investigate different magnetic topological states in AFM half-Heusler materials with the $\mathcal{S}$ symmetry preserved, via the NLHE method.

In this work, we study the NLHE of magnetic topo-

Supported by the National Natural Science Foundation of China (Grant Nos. 11834006, 12074181, and 11674165), the Natural Science Foundation of Jiangsu Province (Grant No. BK20200007), the Fok Ying-Tong Education Foundation of China (Grant No. 161006), and the Fundamental Research Funds for the Central Universities (Grant No. 020414380149).
†They contributed equally to this work.
*Corresponding author. Email: zhanghj@nju.edu.cn
© 2021 Chinese Physical Society and IOP Publishing Ltd

logical states in AFM half-Heusler materials. Firstly, based on the standard effective Luttinger Hamiltonian, we begin with the nonmagnetic parent states, and treat the AFM order as a perturbation in order to calculate electronic structures and phase diagrams under different AFM orders. Next, using symmetry analysis, we derive the independent, symmetry-permitted, nonvanishing components of the BCD tensor. Finally, we focus on TP and Weyl semimetal phases to explicitly calculate the BCD. A prominent peak of BCD is found near the Weyl points (WPs), while no pronounced BCD features are found for TPs; our results are further verified by calculations based on low-energy effective Hamiltonians near these band crossing points.

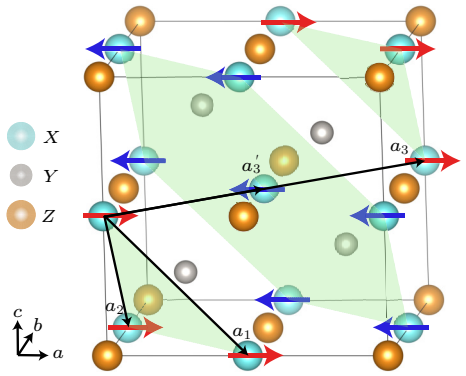

Fig. 1. Crystalline structure and magnetic order of half-Heusler materials XYZ. X and Z atoms form the NaCl-type substructure, and Y and Z atoms form the zinc-blende substructure. Magnetic moments are generated by the X atoms, and the magnetic moments are schematically shown by arrows. Note that the magnetic moments align ferromagnetically in the layer perpendicular to the [111] direction, and antiferromagnetically between two adjacent layers, in the typical G-type AFM. In the absence of the magnetic order, $\boldsymbol{a}_1$, $\boldsymbol{a}_2$, $\boldsymbol{a}_3'$ constitute the lattice basis vectors. With respect to the AFM order, the lattice vector along the $\boldsymbol{a}_3'$ direction is doubled. The new lattice basis vectors are labeled as $\boldsymbol{a}_1$, $\boldsymbol{a}_2$, and $\boldsymbol{a}_3 = 2\boldsymbol{a}_3'$.

Topological Phases. Half-Heusler compounds labeled by XYZ are a group of materials which have been extensively studied, particularly in relation to topological states.[30,54] The compound's crystalline structure is shown in Fig. 1, where X and Z atoms form the NaCl-type substructure, and Y and Z atoms form the zinc-blende substructure. In the absence of AFM order, the crystal space group and corresponding point group are $F\bar{4}3m$ and T_d, respectively. Here, $\boldsymbol{a}_1$, $\boldsymbol{a}_2$, and $\boldsymbol{a}_3'$ are the original lattice basis vectors. With regard to the AFM order, the lattice vectors and unit cell are doubled along the $\boldsymbol{a}_3'$ direction. The new lattice vectors are labeled as $\boldsymbol{a}_1$, $\boldsymbol{a}_2$, and $\boldsymbol{a}_3 = 2\boldsymbol{a}_3'$. For AFM half-Heusler materials, such as GdPtBi, magnetic moments are generated primarily by the X atoms, and align ferromagnetically in one layer which is perpendicular to the [111] direction, and antiferromagnetically between two adjacent layers, in the G-type AFM order.

Similarly to the zinc-blende semiconductors, such as HgTe, the electronic structure around the Fermi level of nonmagnetic half-Heusler materials is dominated by the Γ_8 bands.[13] The Γ_8 bands form a four-fold degeneracy at the Γ point, protected by time-reversal symmetry and the T_d group. Along the C_{3v} axis (e.g., the [111] direction), the Γ_8 bands split into one doubly degenerate band, Λ_6, protected by C_{3v} symmetry, and two nondegenerate bands, $\Lambda_{4,5}$, due to the inversion symmetry breaking of the T_d group. This low-energy band structure is effectively described by the Luttinger Hamiltonian H_0[55] plus a linear bulk inversion-asymmetry (BIA) term, $H_{\rm BIA}$:[13,56]

$$H_0(\boldsymbol{k}) = h_0 + \sum_{i=1}^{5} h_i \Gamma_i, \tag{1a}$$

$$H_{\rm BIA}(\boldsymbol{k}) = \frac{2}{\sqrt{3}} C(k_x V_x + k_y V_y + k_z V_z). \tag{1b}$$

Here, $h_0 = E_v - \beta_c\gamma_1 k^2$, $h_1 = \beta_c\gamma_2(2k_z^2 - k_\parallel^2)$, $h_2 = \sqrt{3}\beta_c\gamma_2 K^2$, $h_3 = 2\sqrt{3}\beta_c\gamma_3 k_x k_y$, $h_4 = 2\sqrt{3}\beta_c\gamma_3 k_x k_z$, $h_5 = 2\sqrt{3}\beta_c\gamma_3 k_y k_z$, $\Gamma_1 = \frac{1}{3}(2J_z^2 - J_x^2 - J_y^2)$, $\Gamma_2 = \frac{1}{\sqrt{3}}(J_x^2 - J_y^2)$, $\Gamma_3 = \frac{2}{\sqrt{3}}J_{xy}$, $\Gamma_4 = \frac{2}{\sqrt{3}}J_{zx}$, and $\Gamma_5 = \frac{2}{\sqrt{3}}J_{yz}$. J_i $(i = x, y, z)$ denotes spin-3/2 matrices (see the explicit matrix form in the Supplementary Material), $J_{ij} = \frac{1}{2}\{J_i, J_j\}$, $V_x = \frac{1}{2}\{J_x, J_y^2 - J_z^2\}$, $V_y = \frac{1}{2}\{J_y, J_z^2 - J_x^2\}$, $V_z = \frac{1}{2}\{J_z, J_x^2 - J_y^2\}$, and $\beta_c = \hbar^2/(2m')$; m' is the effective mass of the Γ_6 bands near the Γ point, $k^2 = k_x^2 + k_y^2 + k_z^2$, $k_\parallel^2 = k_x^2 + k_y^2$, $K^2 = k_x^2 - k_y^2$, and $\{\ \}$ represents the anti-commutator. The AFM order is treated as a perturbation, and in the basis of Γ_8 bands, is given by[40]

$$H_{\rm AFM}(\boldsymbol{M}) = \xi_0 + \sum_{i=1}^{5} \xi_i \Gamma_i, \tag{2}$$

where the explicit expressions for the ξ_i parameters are as given in the Supplementary Material. Based on the low-energy effective Hamiltonian, the band structures and phase diagrams under different directions of AFM moments can be easily obtained.[40] Here, we start from the nonmagnetic phase, then focus on typical cases with lowered symmetries, where the magnetic moments are in the C_{3v} axis, parallel to mirror planes, and in a general direction, respectively.

In the nonmagnetic parent phase without AFM order, a pair of symmetry-protected TPs are present along each C_{3v} axis, as exemplified by the band structure along the [111] direction, as shown in Fig. 2(a), with detailed parameters provided in Table S1 in the Supplementary Material. Two TPs are formed by a doubly degenerate downward Λ_6 band, and a nondegenerate upward Λ_5 (Λ_4) band, belonging to two-dimensional and one-dimensional irreducible representations of the C_{3v} point group, respectively.

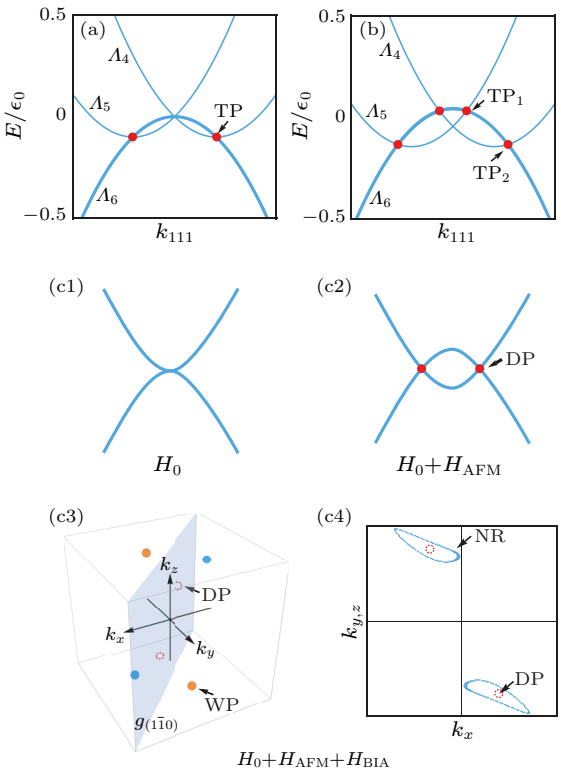

Fig. 2. (a) Band structure along the [111] direction for nonmagnetic half-Heusler materials, based on the $H_0 + H_{\rm BIA}$ model. Here, ϵ_0 is chosen as the energy unit (see Table S2 in the Supplementary Material). A pair of C_{3v} symmetry-protected TPs are marked by red points. (b) The band structure along the [111] direction for AFM half-Heusler materials with magnetic moments in the [111] direction. Note that the C_{3v} symmetry is preserved. The AFM perturbation only pulls away the Λ_6 and $\Lambda_{4,5}$ bands, generating one more pair of TPs, also marked by red points. (c) Weyl semimetal and nodal-line semimetal phases of AFM half-Heusler materials with magnetic moments in the [110] and [100] directions. (c1) The schematic band structure of the H_0 model. A schematic of the band structure of the Dirac semimetal phase is given in (c2), based on the $H_0 + H_{\rm AFM}$ model. DPs are marked by red filled circles. When the BIA term is further introduced, each DP splits into a pair of WPs, or evolves into an NR, depending on the magnetic moment's direction. The Weyl semimetal phase is given in (c3), with the AFM magnetic moments in the [110] direction. The blue and orange colors denote the chirality of WPs. The nodal-line semimetal phase is given in (c4), with the AFM magnetic moments in the [100] direction. The red dashed circles in (c3) and (c4) represent the DPs in (c2).

When the AFM magnetic moments occur along the high-symmetry C_{3v} axis (e.g., the [111] direction), the $C_{3,[111]}$ rotational symmetry is preserved, while all mirror symmetries in C_{3v} are explicitly broken; due to the fractional translation, they are instead replaced by glide symmetries. Nevertheless, the point group is still C_{3v}; as such, the degeneracy of each band remains the same. In fact, we find that the AFM perturbation only shifts and pulls away the Λ_6 and $\Lambda_{4,5}$ bands, as shown in Fig. 2(b) (detailed parameters are listed in Table S2 in the Supplementary Material), leading to the breaking of the fourfold generation at the Γ point, and generating one more pair of TPs. This is consistent with previous calculations.[36] These TPs belong to type B, which is characterized by the presence of more than one nodal line connecting them, with the π Berry phase of a loop encircling each nodal line.[57]

When the magnetic moments are applied within a mirror plane, i.e., α [$\alpha = (1\bar{1}0)$, $(10\bar{1})$, or $(01\bar{1})$], but away from the [111] direction, e.g., along [110], only the glide symmetry, g_α, is preserved, and other symmetries are broken. In this case, the TPs along the C_{3v} axes in the nonmagnetic phase are gapped or split into WPs. To illustrate this, in Fig. 2(c3), we choose representative parameters (see Table S3 in the Supplementary Material), and schematically plot the locations of the WPs. This can be understood as follows: If we neglect the inversion-symmetry breaking BIA term, the combination of the inversion symmetry and the $\mathcal{S}$ symmetry will lead to double degeneracy for each band. The energy of the total Hamiltonian, $H_0(\boldsymbol{k}) + H_{\rm AFM}$, can be solved as follows:

$$E_\pm(\boldsymbol{k}) = (h_0 + \xi_0) \pm \sqrt{\sum_{i=1}^{5}(h_i + \xi_i)^2}. \tag{3}$$

A Dirac semimetal phase is expected when $h_i + \xi_i = 0$ for all $i = 1, 2, \ldots, 5$, as schematically shown in Fig. 2(c2). The phase diagram of the Dirac semimetal phase as a function of ξ_3/ϵ_0 and ξ_4/ϵ_0 turns out to be a critical line.[40] When including the inversion-symmetry breaking BIA term, each Dirac point (DP) will split into WPs, owing to the lifting of Kramer's degeneracy, as schematically shown in Fig. 2(c3).

When the magnetic moments occur along a generic direction, e.g., the [100] direction, all symmetries of C_{3v} are broken. Similarly, without the inversion-breaking BIA term, the system exhibits a Dirac semimetal phase when all the $h_i + \xi_i = 0$ for $i = 1, 2, \ldots, 5$ (see Table S4 in the Supplementary Material), and where the two DPs are located at the $k_y = k_z$ plane. Once the inversion-breaking BIA term is included, the DPs evolve into two nodal rings (NRs), schematically shown in Fig. 2(c4), leading to a nodal-line semimetal phase.

Berry Curvature Dipole. Firstly, we provide a brief overview of the NLHE. For a time-reversal-invariant system, an oscillating electric field $E(t) = \mathrm{Re}\{\mathcal{E}e^{i\omega t}\}$ will induce a second-order nonlinear response current, $j_a^{2\omega} = \chi_{\rm abc}\mathcal{E}_b\mathcal{E}_c$, with the response coefficient, $\chi_{\rm abc}$, given by[42]

$$\chi_{\rm abc} = -\varepsilon_{\rm adc}\frac{e^3\tau}{2(1+i\omega\tau)}D_{\rm bd}, \tag{4}$$

where $\varepsilon_{\rm adc}$ is the third-rank Levi-Civita tensor, τ is the relaxation time, and

$$D_{\rm bd} = \int f_0(\partial_b\Omega_{\rm d})\boldsymbol{dk} \tag{5}$$

is the dipole moment of the Berry curvature $\Omega_{\rm d}$ over the occupied states, referred to as BCD. Here, f_0 represents the equilibrium Fermi-Dirac distribution. Note that since the BCD density, $d_{\rm bd}(\boldsymbol{k}) \equiv \partial_b \Omega_{\rm d}(\boldsymbol{k})$, is odd under inversion symmetry, $D_{\rm bd}$ vanishes in the presence of inversion symmetry, leading to the absence of a nonlinear Hall response. In contrast, $d_{\rm bd}(\boldsymbol{k})$ is even under the time-reversal symmetry, so that $D_{\rm bd}$ and the corresponding NLHE persist in time-reversal-invariant systems with the breaking of inversion symmetry. It is worth mentioning that a requirement of time-reversal symmetry is to exclude the contribution to the nonlinear Hall current of semiclassical terms which have nothing to do with the BCD.[42]

Intriguingly, for AFM materials with broken time-reversal symmetry, as long as they possess the $\mathcal{S}$ symmetry, which is a combination of time-reversal symmetry and fractional translation, the BCD density $d_{\rm bd}(\boldsymbol{k})$ satisfies $\mathcal{S} d_{\rm bd}(\boldsymbol{k}) = d_{\rm bd}(-\boldsymbol{k})$. This means that $\mathcal{S}$ symmetry plays the same role as time-reversal symmetry for the BCD, such that Eq. (4) still holds for these AFM materials.[53] Taking into account that such $\mathcal{S}$ symmetry exists in noncentrosymmetric AFM half-Heusler materials, one expects to observe BCD-origin NLHEs.

Table 1. Properties of k_i and Ω_i under several important symmetry operations in the C_{3v} group.

	k_x	k_y	k_z	Ω_x	Ω_y	Ω_z
$g_{(1\bar{1}0)}$	k_y	k_x	k_z	$-\Omega_y$	$-\Omega_x$	$-\Omega_z$
$g_{(10\bar{1})}$	k_z	k_y	k_x	$-\Omega_z$	$-\Omega_y$	$-\Omega_x$
$g_{(01\bar{1})}$	k_x	k_z	k_y	$-\Omega_x$	$-\Omega_z$	$-\Omega_y$
$C_{3,[111]}$	k_z	k_x	k_y	Ω_z	Ω_x	Ω_y

Point-group symmetries impose further constraints on the BCD tensor, $D_{\rm bd}$, and force some components to vanish. In Table 1, we list the transformation properties of k_i and Ω_i, where $i = x, y, z$, under several important symmetry operations of the C_{3v} group in the Cartesian coordinate for AFM half-Heusler materials. According to Table 1, when the magnetic moments are in the [111] direction, preserving the C_{3v} group, we find that $D_{xy} = -D_{yx} = D_{yz} = -D_{zy} = D_{zx} = -D_{xz}$ and the rest components vanish, because their BCD density is odd under at least one of the symmetry operations. This means that only one of the nine components of $D_{\rm bd}$ is independent in this case. When the magnetic moments are in the [110] direction, only one glide symmetry $g_{(1\bar{1}0)}$ is preserved. According to Table 1, we obtain $D_{xx} = -D_{yy}$, $D_{zz} = 0$, $D_{xy} = -D_{yx}$, $D_{zx} = -D_{zy}$, and $D_{xz} = -D_{yz}$, resulting in four independent components. If the magnetic moments are in the [100] direction, which breaks all symmetries in the C_{3v} group, all nine BCD components persist, and are generally independent from one another. Moreover, for the nonmagnetic phase belonging to the T_d group, symmetries force all BCD components to vanish in the same way.[48] As a result, depending on the directions of the AFM moments, different nonvanishing and independent BCD components are expected, due to the gradually lowered symmetry, as summarized in Table 2. Therefore, the nonzero BCD components obtained via experimental NLHE measurements can be used to determine whether the AFM moments are in a high-symmetry axis, within high symmetry planes, or in a general direction. It should be emphasized that the above symmetry arguments are quite general, and can be applied to a wide class of AFM half-Heusler materials.

Table 2. Numbers of nonzero BCD components and independent BCD components for different magnetic orders.

Magnetic orders	Nonzero	Independent
Nonmagnetic	0	0
$\boldsymbol{M}_{[111]}$	6	1
$\boldsymbol{M}_{[110]}$	8	4
$\boldsymbol{M}_{[100]}$	9	9

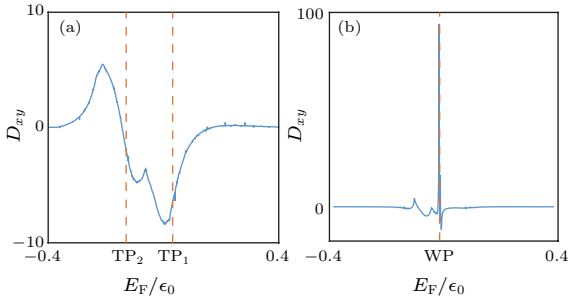

Fig. 3. Calculated BCD component, D_{xy}, with varying Fermi energy, for (a) TP semimetal and (b) Weyl semimetal phases of AFM half-Heusler materials under [111]- and [110]-direction magnetic moments, respectively. A prominent peak of BCD around the WPs is found in the Weyl semimetal phase [see the red dashed line in (b)], while there is no pronounced contribution from TPs in the TP semimetal phase.

Next, we focus on the TP semimetal and Weyl semimetal phases of AFM half-Heusler materials under magnetic moments in the [111] and [110] directions, respectively, so as to explicitly calculate the BCD as a function of energy. According to Eq. (5), two factors, namely, the Fermi distribution f_0 and the BCD density $d_{\rm bd}(\boldsymbol{k})$, are involved in the calculation of $D_{\rm bd}$. For simplicity, the temperature is set to zero, such that $f_0(\boldsymbol{k}) = 1/0$ for occupied/unoccupied states. In addition, the Berry curvature of the ith band can be obtained via the following formula:[58]

$$\Omega^a_{i\boldsymbol{k}} = -2\varepsilon^{abc} \sum_{j \neq i} \frac{{\rm Im}\langle i|\partial_{k_b}\hat{\mathcal{H}}|j\rangle\langle j|\partial_{k_c}\hat{\mathcal{H}}|i\rangle}{(\epsilon^i_{\boldsymbol{k}} - \epsilon^j_{\boldsymbol{k}})^2}, \quad (6)$$

where $a, b, c = x, y, z$, and i, j are band indices. Here the low-energy physics of the AFM half-Heusler materials can be properly described by the effective $k \cdot p$ Luttinger model around the Γ point, so the BCD can be simply calculated by the effective model, without

involving the full Brillouin zone. Taking D_{xy} as an example, which corresponds to $j_x^{2\omega} = \chi_{xxz}\mathcal{E}_x\mathcal{E}_z$, our results are shown in Fig. 3, where the parameters for the calculations are listed in Tables S2 and S3 in the Supplementary Material. A prominent peak of BCD around WPs is found in the Weyl semimetal phase, while there is no pronounced contribution from TPs in TP semimetal phase. There are some weak peaks around the TPs, which are primarily contributed by other trivial Fermi pockets.

We further analyze the contributions of TPs and WPs, based on the local general Hamiltonian near these band crossing points. The contributions of WPs have been discussed in previous works,[42,46–48] which point out that the magnitude of the BCD can be tuned by the tilt of the Weyl cone. Type-B TPs can be described by the low-energy effective Hamiltonian, expanded to a linear order around the TPs:[59]

$$H = \begin{pmatrix} E_0 + Ak_z & 0 & Dk_y & Dk_x \\ 0 & -E_0 + Ak_z & F^*k_x & -F^*k_y \\ D^*k_y & Fk_x & Bk_z + Ck_x & Ck_y \\ D^*k_x & -Fk_y & Ck_y & Bk_z - Ck_x, \end{pmatrix}. \tag{7}$$

Here, $A, B, C, D(D^*), E_0, F(F^*)$ are parameters, and the C_{3v} direction [111] is chosen as the k_z axis. For doubly degenerate bands belonging to the two-dimensional representation in the k_z direction, the low-energy Hamiltonian around each TP in the k_x–k_y plane to linear order is given by

$$H = Bk_z\sigma_0 + Ck_x\sigma_z + Ck_y\sigma_x, \tag{8}$$

which clearly leads to vanishing Berry curvatures. For the two nondegenerate bands, the low-energy Hamiltonian to linear order is given by

$$H = Ak_z\sigma_0 + E_0\sigma_z, \tag{9}$$

which also gives rise to zero Berry curvatures. Therefore, we would expect the TPs to make no contribution to the BCD, which explains the numerical results above.

In summary, we have investigated the NLHE in AFM half-Heusler materials. Based on the effective model method, we have systematically studied their electronic structure and phase diagrams. Due to the constraints on the BCD tensor by symmetries, some elements of the BCD tensor survive for AFM half-Heusler materials. A prominent peak in the BCD around the WPs is found in the Weyl semimetal phase, while there are no pronounced contributions from TPs in the TP semimetal phase. This is further supported by an analysis based on low-energy effective Hamiltonians. Our work shows that the NLHE method may provide a powerful tool used to characterize magnetic topological states with various AFM configurations in AFM half-Heusler materials.

References

[1] Thouless D J, Kohmoto M, Nightingale M P and den N M 1982 *Phys. Rev. Lett.* **49** 405
[2] Hasan M Z and Kane C L 2010 *Rev. Mod. Phys.* **82** 3045
[3] Qi X L and Zhang S C 2011 *Rev. Mod. Phys.* **83** 1057
[4] Koenig M, Wiedmann S, Bruene C, Roth A, Buhmann H, Molenkamp L W, Qi X L and Zhang S C 2007 *Science* **318** 766
[5] Zhang H, Liu C X, Qi X L, Dai X, Fang Z and Zhang S C 2009 *Nat. Phys.* **5** 438
[6] Yu R, Zhang W, Zhang H J, Zhang S C, Dai X and Fang Z 2010 *Science* **329** 61
[7] Chang C Z, Zhang J, Feng X, Shen J, Zhang Z, Guo M, Li K, Ou Y, Wei P, Wang L L, Ji Z Q, Feng Y, Ji S, Chen X, Jia J, Dai X, Fang Z, Zhang S C, He K, Wang Y, Lu L, Ma X C and Xue Q K 2013 *Science* **340** 167
[8] Wan X, Turner A M, Vishwanath A and Savrasov S Y 2011 *Phys. Rev. B* **83** 205101
[9] Xu G, Weng H, Wang Z, Dai X and Fang Z 2011 *Phys. Rev. Lett.* **107** 186806
[10] Wang Z, Sun Y, Chen X Q, Franchini C, Xu G, Weng H, Dai X and Fang Z 2012 *Phys. Rev. B* **85** 195320
[11] Wang Z, Weng H, Wu Q, Dai X and Fang Z 2013 *Phys. Rev. B* **88** 125427
[12] Weng H, Fang C, Fang Z, Bernevig B A and Dai X 2015 *Phys. Rev. X* **5** 011029
[13] Ruan J, Jian S K, Yao H, Zhang H, Zhang S C and Xing D 2016 *Nat. Commun.* **7** 11136
[14] Bradlyn B, Cano J, Wang Z, Vergniory M G, Felser C, Cava R J and Bernevig B A 2016 *Science* **353** aaf5037
[15] Armitage N P, Mele E J and Vishwanath A 2018 *Rev. Mod. Phys.* **90** 015001
[16] Fu L and Kane C L 2008 *Phys. Rev. Lett.* **100** 096407
[17] Qi X L, Hughes T L, Raghu S and Zhang S C 2009 *Phys. Rev. Lett.* **102** 187001
[18] Sun H H, Zhang K W, Hu L H, Li C, Wang G Y, Ma H Y, Xu Z A, Gao C L, Guan D D, Li Y Y, Liu C, Qian D, Zhou Y, Fu L, Li S C, Zhang F C and Jia J F 2016 *Phys. Rev. Lett.* **116** 257003
[19] Zhang P, Yaji K, Hashimoto T, Ota Y, Kondo T, Okazaki K, Wang Z, Wen J, Gu G D, Ding H and Shin S 2018 *Science* **360** 182
[20] Fang Y, Pan J, Zhang D, Wang D, Hirose H T, Terashima T, Uji S, Yuan Y, Li W, Tian Z, Xue J, Ma Y, Zhao W, Xue Q, Mu G, Zhang H and Huang F 2019 *Adv. Mater.* **31** 1901942
[21] Yuan Y, Pan J, Wang X, Fang Y, Song C, Wang L, He K, Ma X, Zhang H, Huang F, Li W and Xue Q K 2019 *Nat. Phys.* **15** 1046
[22] Mong R S K, Essin A M and Moore J E 2010 *Phys. Rev. B* **81** 245209
[23] Zhang D, Shi M, Zhu T, Xing D, Zhang H and Wang J 2019 *Phys. Rev. Lett.* **122** 206401
[24] Li J, Li Y, Du S, Wang Z, Gu B L, Zhang S C, He K, Duan W and Xu Y 2019 *Sci. Adv.* **5** eaaw5685
[25] Xu Y, Song Z, Wang Z, Weng H and Dai X 2019 *Phys. Rev. Lett.* **122** 256402
[26] Liu C, Wang Y, Li H, Wu Y, Li Y, Li J, He K, Xu Y, Zhang J and Wang Y 2020 *Nat. Mater.* **19** 522

[27] Zhang J, Wang D, Shi M, Zhu T, Zhang H and Wang J 2020 *Chin. Phys. Lett.* **37** 077304
[28] Wang H, Wang D, Yang Z, Shi M, Ruan J, Xing D, Wang J and Zhang H 2020 *Phys. Rev. B* **101** 081109(R)
[29] Wieder B J, Kim Y, Rappe A M and Kane C L 2016 *Phys. Rev. Lett.* **116** 186402
[30] Lin H, Wray L A, Xia Y, Xu S, Jia S, Cava R J, Bansil A and Hasan M Z 2010 *Nat. Mater.* **9** 546
[31] Chadov S, Qi X, Kuebler J, Fecher G H, Felser C and Zhang S C 2010 *Nat. Mater.* **9** 541
[32] Xiao D, Yao Y, Feng W, Wen J, Zhu W, Chen X Q, Stocks G M and Zhang Z 2010 *Phys. Rev. Lett.* **105** 096404
[33] Al-Sawai W, Lin H, Markiewicz R S, Wray L A, Xia Y, Xu S Y, Hasan M Z and Bansil A 2010 *Phys. Rev. B* **82** 125208
[34] Yan B and de Visser A 2014 *MRS Bull.* **39** 859
[35] Hirschberger M, Kushwaha S, Wang Z, Gibson Q, Liang S, Belvin C A, Bernevig B A, Cava R J and Ong N P 2016 *Nat. Mater.* **15** 1161
[36] Yang H, Yu J, Parkin S S P, Felser C, Liu C X and Yan B 2017 *Phys. Rev. Lett.* **119** 136401
[37] Cano J, Bradlyn B, Wang Z, Hirschberger M, Ong N P and Bernevig B A 2017 *Phys. Rev. B* **95** 161306
[38] Shekhar C, Kumar N, Grinenko V, Singh S, Sarkar R, Luetkens H, Wu S C, Zhang Y, Komarek A C, Kampert E, Skourski Y, Wosnitza J, Schnelle W, McCollam A, Zeitler U, Kübler J, Yan B, Klauss H H, Parkin S S P and Felser C 2018 *Proc. Natl. Acad. Sci. USA* **115** 9140
[39] Suzuki T, Chisnell R, Devarakonda A, Liu Y T, Feng W, Xiao D, Lynn J W and Checkelsky J G 2016 *Nat. Phys.* **12** 1119
[40] Yu J, Yan B and Liu C X 2017 *Phys. Rev. B* **95** 235158
[41] Klitzing K V, Dorda G and Pepper M 1980 *Phys. Rev. Lett.* **45** 494
[42] Sodemann I and Fu L 2015 *Phys. Rev. Lett.* **115** 216806
[43] Du Z Z, Wang C M, Lu H Z and Xie X C 2018 *Phys. Rev. Lett.* **121** 266601
[44] Zhang Y, van den Brink J, Felser C and Yan B 2018 *2D Mater.* **5** 044001
[45] You J S, Fang S, Xu S Y, Kaxiras E and Low T 2018 *Phys. Rev. B* **98** 121109
[46] Facio J I, Efremov D, Koepernik K, You J S, Sodemann I and van den Brink J 2018 *Phys. Rev. Lett.* **121** 246403
[47] Zhang Y, Sun Y and Yan B 2018 *Phys. Rev. B* **97** 041101
[48] Chen C, Wang H, Wang D and Zhang H 2019 *SPIN* **09** 1940017
[49] Xu S Y, Ma Q, Shen H, Fatemi V, Wu S, Chang T R, Chang G, Valdivia A M M, Chan C K, Gibson Q D, Zhou J, Liu Z, Watanabe K, Taniguchi T, Lin H, Cava R J, Fu L, Gedik N and Jarillo-Herrero P 2018 *Nat. Phys.* **14** 900
[50] Kang K, Li T, Sohn E, Shan J and Mak K F 2018 arXiv:1809.08744 [cond-mat.mes-hall]
[51] Ma Q, Xu S Y, Shen H, MacNeill D, Fatemi V, Chang T R, Mier V A M, Wu S, Du Z, Hsu C H, Fang S, Gibson Q D, Watanabe K, Taniguchi T, Cava R J, Kaxiras E, Lu H Z, Lin H, Fu L, Gedik N and Jarillo-Herrero P 2019 *Nature* **565** 337
[52] Son J, Kim K H, Ahn Y H, Lee H W and Lee J 2019 *Phys. Rev. Lett.* **123** 036806
[53] Shao D F, Zhang S H, Gurung G, Yang W and Tsymbal E Y 2020 *Phys. Rev. Lett.* **124** 067203
[54] Graf T, Parkin S S P and Felser C 2011 *IEEE Trans. Magn.* **47** 367
[55] Zhang D, Wang H, Ruan J, Yao G and Zhang H 2018 *Phys. Rev. B* **97** 195139
[56] Dai X, Hughes T L, Qi X L, Fang Z and Zhang S C 2008 *Phys. Rev. B* **77** 125319
[57] Zhu Z, Winkler G W, Wu Q, Li J and Soluyanov A A 2016 *Phys. Rev. X* **6** 031003
[58] Xiao D, Chang M C and Niu Q 2010 *Rev. Mod. Phys.* **82** 1959
[59] Winkler G W, Wu Q, Troyer M, Krogstrup P and Soluyanov A A 2016 *Phys. Rev. Lett.* **117** 076403

Supplementary Material: Nonlinear Hall Effect in Antiferromagnetic Half-Heusler Materials

Cheng Chen[1†], Huaiqiang Wang[1†], Zhilong Yang[1], and Haijun Zhang[1,2*]
[1] *National Laboratory of Solid State Microstructures, School of Physics, Nanjing University, Nanjing 210093, China*
[2] *Collaborative Innovation Center of Advanced Microstructures, Nanjing University, Nanjing 210093, China*[*]
(Dated: April 26, 2021)

TABLE S1. Parameters for Fig. 2(a), where a is a real parameter with the unit of length.

$\frac{E_v+\xi_0}{\xi_0}$	γ_1	γ_2	γ_3	$\frac{C}{\beta_c/a}$
0	0	0.5	0.1	0.2

TABLE S2. Parameters for Fig. 2(b) and Fig. 3(a). Here, $\xi_1 = 0$, $\xi_2 = 0$, $\xi_3 = \xi_4 = \xi_5 = \xi$. The energy unit ϵ_0 is defined as $\epsilon_0 \equiv \beta_c/a^2$.

$\frac{E_v+\xi_0}{\xi_0}$	γ_1	γ_2	γ_3	$\frac{C}{\beta_c/a}$	$\frac{\xi}{\epsilon_0}$
0	0	0.5	0.1	0.2	−0.025

TABLE S3. Parameters for Fig. 2(c3) and Fig. 3(b). Here, $\xi_2 = 0$, $\xi_4 = \frac{\sqrt{3}\gamma_3\xi_1\xi_3+\gamma_2\xi_3^2}{\sqrt{\gamma_2}}$, $\xi_5 = \xi_4$.

$\frac{E_v+\xi_0}{\xi_0}$	γ_1	γ_2	γ_3	$\frac{C}{\beta_c/a}$	$\frac{\xi_1}{\epsilon_0}$	$\frac{\xi_3}{\epsilon_0}$
0	0	0.5	0.1	0.2	−0.16	−0.01

TABLE S4. Parameters for Fig. 2(c4), $\xi_4 = \xi_3$, $\xi_1 = \gamma_2\frac{\xi_5^2-\xi_3^2}{2\sqrt{3}\gamma_3\xi_5}$, $\xi_2 = -\sqrt{3}\xi_1$.

$\frac{E_v+\xi_0}{\xi_0}$	γ_1	γ_2	γ_3	$\frac{C}{\beta_c/a}$	$\frac{\xi_3}{\epsilon_0}$	$\frac{\xi_5}{\epsilon_0}$
0	0	0.5	0.1	0.02	0.001	−0.002

I. PARAMETERS IN THE $k\cdot p$ MODEL

This section is a summary of parameters listed in Table S1, S2, S3, and S4 for the models used in the main text.

II. EXPLICIT FORM OF SPIN-3/2 MATRICES AND ξ_i PARAMETERS IN THE HAMILTONIAN

The matrix form of the spin-3/2 matrices is given by

$$J_x = \frac{1}{2}\begin{pmatrix} 0 & \sqrt{3} & 0 & 0 \\ \sqrt{3} & 0 & 2 & 0 \\ 0 & 2 & 0 & \sqrt{3} \\ 0 & 0 & \sqrt{3} & 0 \end{pmatrix}, \tag{1a}$$

$$J_y = \frac{\mathrm{I}}{2}\begin{pmatrix} 0 & -\sqrt{3} & 0 & 0 \\ \sqrt{3} & 0 & -2 & 0 \\ 0 & 2 & 0 & -\sqrt{3} \\ 0 & 0 & \sqrt{3} & 0 \end{pmatrix}, \tag{1b}$$

$$J_z = \frac{1}{2}\begin{pmatrix} 3 & 0 & 0 & 0 \\ 0 & 1 & 0 & 0 \\ 0 & 0 & -1 & 0 \\ 0 & 0 & 0 & -3 \end{pmatrix}. \tag{1c}$$

The expressions for ξ_i $(i = 0, 1, 2, 3, 4, 5)$ are polynomials of magnetic moment $\mathbf{M}$, listed as follows: [1]

$$\begin{aligned}
\xi_0 =& \alpha_1\left(M_x^2+M_y^2+M_z^2\right)+\beta_1\left(M_yM_z+M_zM_x+M_xM_y\right),\\
\xi_1 =& \alpha_3\left(2M_z^2-M_x^2-M_y^2\right)+\beta_3\left(2M_xM_y-M_yM_z-M_zM_x\right),\\
\xi_2 =& \alpha_3\sqrt{3}\left(M_x^2-M_y^2\right)+\beta_3\sqrt{3}\left(M_yM_z-M_xM_z\right),\\
\xi_3 =& \alpha_2\left(M_x^2+M_y^2+M_z^2\right)+\beta_2\left(M_yM_z+M_zM_x+M_xM_y\right)+2[\alpha_4\left(2M_z^2-M_x^2-M_y^2\right)+\beta_4\left(2M_xM_y-M_yM_z-M_zM_x\right)],\\
\xi_4 =& \alpha_2\left(M_x^2+M_y^2+M_z^2\right)+\beta_2\left(M_yM_z+M_zM_x+M_xM_y\right)-\left[\alpha_4\left(2M_z^2-M_x^2-M_y^2\right)+\beta_4\left(2M_xM_y-M_yM_z-M_zM_x\right)\right]\\
&-\sqrt{3}\left[\alpha_4\sqrt{3}\left(M_x^2-M_y^2\right)+\beta_4\sqrt{3}\left(M_yM_z-M_xM_z\right)\right],\\
\xi_5 =& \alpha_2\left(M_x^2+M_y^2+M_z^2\right)+\beta_2\left(M_yM_z+M_zM_x+M_xM_y\right)-\left[\alpha_4\left(2M_z^2-M_x^2-M_y^2\right)+\beta_4\left(2M_xM_y-M_yM_z-M_zM_x\right)\right]\\
&+\sqrt{3}\left[\alpha_4\sqrt{3}\left(M_x^2-M_y^2\right)+\beta_4\sqrt{3}\left(M_yM_z-M_xM_z\right)\right].
\end{aligned} \tag{2}$$

[1] J. Yu, B. Yan, and C.-X. Liu, Phys. Rev. B **95**, 235158 (2017).

* zhanghj@nju.edu.cn